

## Global Energetics of Solar Flares. XII. Physical Scaling Laws

MARKUS J. ASCHWANDEN<sup>1</sup>

<sup>1</sup>*Solar and Stellar Astrophysics Laboratory (LMSAL), Palo Alto, CA 94304, USA*

### ABSTRACT

In this study we test 30 variants of 5 physical scaling laws that describe different aspects of solar flares. We express scaling laws in terms of the magnetic potential field energy  $E_p$ , the mean potential field strength  $B_p$ , the free energy  $E_{free}$ , the dissipated magnetic flare energy  $E_{diss}$ , the mean loop length scale  $L$ , the mean helically twisted flux tube radius  $R$ , the sunspot radius  $r$ , the emission measure-weighted flare temperature  $T_w$ , the electron density  $n_e$ , and the total emission measure  $EM$ , measured from a data set of  $\lesssim 400$  GOES M- and X-class flare events. The 5 categories of physical scaling laws include (i) a scaling law of the potential-field energy, (ii) a scaling law for helical twisting, (iii) a scaling law for Petschek-type magnetic reconnection, (iv) the Rosner-Tucker-Vaiana scaling law, and (v) the Shibata-Yokoyama scaling law. We test the self-consistency of these theoretical scaling laws with observed parameters by requiring two conditions: a cross-correlation coefficient of  $CCC > 0.5$  between the observed and theoretically predicted scaling laws, and a linear regression fit with a slope of  $\alpha \approx 1$ . With these two criteria we find that 10 out of the 30 tested scaling law variants are consistent with the observed data, which strongly corroborates the existence and validity of the tested flare scaling laws.

*Keywords:* Solar flares — Scaling laws

### 1. INTRODUCTION

Scaling laws describe physical models with functional (mathematical) relationships between physical quantities that scale with each other over a significant parameter range, often in form of power laws, e.g.,  $X = a^\alpha b^\beta c^\gamma$ , where  $X, a, b, c$  are physical quantities, and  $\alpha, \beta, \gamma$  are power law exponents. The choice of relevant parameters ( $X, a, b, c$ ) requires the knowledge of specific physical models, while the power law exponents ( $\alpha, \beta, \gamma$ ) can either be predicted by a physical model, or be obtained from forward-fitting of purely mathematical (power law) functions. Obviously, since the latter method provides a physics-free parameterization only, it should be discouraged in favor of fitting specific physical models.

A tricky player in any forward-fitting method is the data noise and the uncertainty of measured observables. The larger the data noise level is, the larger is the resulting uncertainty of the fitted power law exponents. Vice versa, the best-fit power law exponents may be strongly biased if some physical parameters are dominated by noise. In this study we use analytically derived scaling laws and self-consistency tests with observations, rather than fitting empirical power law exponents that by themselves do not reveal the underlying physical processes. The identification of relevant scaling laws often requires 3-D models of observed 2-D features (e.g., review of Aschwanden 2010). One of the motivations of this study is the identification of physical parameters that are most relevant for solar flare prediction (machine-learning) methods.

There are numerous studies on scaling laws of solar flares and coronal heating, of which we mention here a few representative examples: The Rosner-Tucker-Vaiana law applied to solar flares (Rosner et al. 1978; Aschwanden and Shimizu 2013); scaling laws of electron time-of-flight distances and loop lengths (Aschwanden et al. 1996); scaling laws of soft X-ray measurements in solar flares (Garcia 1998); scaling laws of the coronal magnetic field and loop length in solar and stellar flares (Yokoyama and Shibata 1998; Shibata and Yokoyama 1999, 2002; Yamamoto et

Corresponding author: Markus J. Aschwanden  
 aschwanden@lmsal.com

al. 2002); Aschwanden et al. 2008; Namekata et al. 2017); scaling laws for a nanoflare-heated solar corona (Vekstein and Katsukawa 2000); scaling laws from solar nanoflares to stellar giant flares (Aschwanden 2007); scaling laws and frequency distributions in self-organized criticality models of solar flares (Morales and Charbonneau 2008); universal scaling of space and temporal parameters in solar flares (Aschwanden et al. 2013); scaling laws of quasi-periodic pulsation periods and flare durations (Pugh et al. 2019); scaling law between solar energetic particle events and solar flares (Kahler 2013).

In this study we are using a total of  $\approx 20$  physical parameters, mostly unmeasured before, with large statistics (172 magnetic or 391 non-magnetic flare events), with detailed descriptions in a series of 11 papers on the global energetics of solar flares. We are testing 30 trial scaling laws of solar flares and find 10 scaling laws that are consistent with the observed flare data. Data analysis and the results of the scaling laws are presented in Section 2, a discussion of earlier work in the light of the new results in Section 3, and conclusions in Section 4.

## 2. OBSERVATIONS AND METHODS

### 2.1. *Observations*

The data analysis presented here is mostly based on the measurements of flare parameters published in a series of 11 papers on the global energetics in solar flares and associated *coronal mass ejections (CMEs)*, using observations made with the *Helioseismic and Magnetic Imager (HMI)* (Scherrer et al. 2012) and the *Atmospheric Imaging Assembly (AIA)* (Lemen et al. 2012) onboard the *Solar Dynamics Observatory (SDO)* (Pesnell et al. 2012). In particular we are using magnetic flare parameters of all GOES M- and X-class flares during the first 3.5 years of the SDO mission (2010-2014), which are obtained from 173 flare events that occurred near the solar disk center (within a longitude range of  $\pm 45^\circ$  due to magnetic modeling restrictions), measured in Paper I (Aschwanden, Xu, and Jing 2014a), in Paper X (Aschwanden et al. 2020), and in Paper XI (Aschwanden et al. 2019a). For testing the *Rosner-Tucker-Vaiana (RTV)* law (Section 3.4) we use a more complete data set of 391 flare events located at any heliographic longitude, since no magnetic parameter is necessary for the RTV law.

Magnetic modeling with the *Vertical Current Approximation Non-Linear Force-Free Field (VCA-NLFFF)* code (Aschwanden 2013), which has the capacity of fitting coronal loops in the force-free coronal regime, rather than using the non-forcefree photospheric magnetic vector field of other NLFFF codes (e.g., Wiegmann et al. 2006), yields the following parameters (also called observables here): the mean potential field  $B_p$ , the mean nonpotential field  $B_{np}$ , the mean azimuthal magnetic field component  $B_{free}$  associated with the free energy, the mean dissipated magnetic field during a flare  $B_{diss}$ , the mean potential energy  $E_p$ , the mean nonpotential energy  $E_{np}$ , the mean free energy  $E_{free}$ , the mean dissipated magnetic energy  $E_{diss}$ , the mean helical twist radius  $R$ , the sunspot radial half width  $r$ , the depth of buried magnetic charges  $d$ , the mean magnetic length scale  $L$ , and the flare duration  $\tau_{flare}$ . For testing the RTV scaling law we use five additional parameters: The length scale of thermal flare emission  $L_{th}$ , the emission measure-weighted electron temperature  $T_e$ , the mean electron density of thermal flare emission  $n_e$ , the total thermal emission measure  $EM$ , and the total thermal energy  $E_{th}$ . The minimum and maximum values, as well as the means and standard deviations of these observables of our data sets of 173 (and 391) analyzed events are given in Table 1. The observables will be used here to test scaling law relationships in solar flares. The main difference to previous work is the exclusive testing of scaling laws that are based on specific physical models (of solar flares), rather than determining empirical scaling parameters.

### 2.2. *Method of Testing Scaling Laws*

In this study we aim to identify the physical parameters that are relevant for solar flare and coronal heating processes, as well as to quantify which physical scaling laws are consistent with observations. For self-consistency tests between theoretically predicted and observationally measured scaling laws we use two requirements: (i) a cross-correlation coefficient of  $CCC > 0.5$  between theoretical and observational (logarithmic) parameter values, and (ii) a power law slope of  $\alpha \approx 1$  of the linear regression fit between the (logarithmic) theoretical  $[\log(y)]$  and observational  $[\log(x)]$  parameters, within the statistical uncertainties  $\sigma$  of the linear regression fits,

$$\log[y(x)] = \text{const} + (\alpha \pm \sigma) \log[x] , \quad (1)$$

The statistical uncertainty  $\sigma$  of the linear regression slope  $\alpha$  is defined by the (geometric) mean and (half) difference of the two fits with exchanged axes ( $\log[y(x)]$  and  $\log[x(y)]$ ). We find it to be substantially larger than the uncertainty due to the limited (statistical) number of events. The cases with scaling laws that fulfil the criteria  $CCC > 0.5$  and  $0.8 < \alpha < 1.2$  are marked with grey panels in Figs. 3-5 and 7-8. In the following discussion we will see that such self-consistency tests of scaling laws are mostly lacking in literature.

### 3. DATA ANALYSIS AND RESULTS

#### 3.1. Scaling Law of the Potential-Field Energy

The potential field represents the minimum energy state of a magnetic field (Priest 1975), and thus constitutes also a lower limit of the non-potential magnetic field energy. The total magnetic energy  $E_p$  of a potential field  $\mathbf{B}_p(\mathbf{x})$  is generally expressed by an integral of the (squared) magnetic field strength over a well-defined spatial volume,

$$E_p = \int \left( \frac{B_p^2(x, y, z)}{8\pi} \right) dV = \int \left( \frac{B_p^2(x, y, z)}{8\pi} \right) dx dy dz. \quad (2)$$

This potential energy  $E_p$  can be calculated from the magnetic field at the lower (photospheric) boundary  $z_{phot}(x, y)$  of the computation box, such as given by a line-of-sight magnetogram  $B_z(x, y, z = z_{phot})$ , and from a potential-field extrapolation, which produces a volume-filling magnetic field  $\mathbf{B}(\mathbf{x}) = [B_x(x, y, z), B_y(x, y, z), B_z(x, y, z)]$ .

Potential field calculation methods include the Green's function (Schmidt 1964; Sakurai 1982), the spherical Schmidt method, based on an eigen-function (spherical harmonic) expansion method, using Legendre polynomials (Altschuler and Newkirk 1969), or simply by an iterative decomposition of (sub-photospheric) unipolar magnetic charges (e.g., Aschwanden and Sandman 2010). The latter approach is conceptually the simplest method, where a potential field can be represented by a sum of unipolar magnetic charges, whose field strengths fall off according to the squared-distance law (which also occurs in electric or gravitational potential fields),

$$\mathbf{B}_p(\mathbf{x}) = \sum_{j=1}^{N_m} \mathbf{B}_j(\mathbf{x}) = \sum_{j=1}^{N_m} B_j \left( \frac{\mathbf{r}_j}{d_j} \right)^{-2} \left( \frac{\mathbf{r}_j}{r_j} \right), \quad (3)$$

where  $N_m$  is the number of unipolar magnetic charges,  $\mathbf{r}_j = [(x - x_m), (y - y_m), (z - z_m)]$  is the vector of the magnetic field direction,  $[x_m, y_m, z_m]$  is the location of the buried unipolar magnetic charge (in a Cartesian coordinate system),  $d_j$  is the depth of the subphotospheric magnetic charge, and  $B_j$  is the magnetic field strength at the (photospheric) solar surface, in vertical direction above the location of the unipolar magnetic charge. The squared-distance fall-off of a potential field is equivalent to a divergence-free field, i.e.,  $\nabla \cdot \mathbf{B} = 0$ .

We derive a simple scaling law for the potential energy  $E_p$  of an active region in the solar corona, as a function of the maximum magnetic potential-field strength  $B_p$ , the length scale  $L$  of the magnetic flare area, and the sunspot radius  $r$ . The potential field energy  $E_p$  (Eq. 2) can be approximated by the mean magnetic field strength  $B_p$  in a flare volume  $V$ ,

$$E_p = q_A \left( \frac{B_p^2}{8\pi} \right) V, \quad (4)$$

with  $q_A$  being an empirical scaling factor that can account for various flare geometries.

The flare volume  $V$  can be expressed by the product of the projected flare area  $A$  and the vertical height extent  $H$  of the magnetic volume,

$$V = A H, \quad (5)$$

and a flare length scale  $L$  can be defined from the 2-D flare area  $A$ ,

$$A = L^2. \quad (6)$$

The height  $H$  of the magnetic flare volume can be estimated from the location where the magnetic energy drops to half of the peak value, which is constrained by the distance-square law of the magnetic field  $B(H)$  and the mean depth  $d$  where the unipolar magnetic energies are buried (see Figs. 1 and 2),

$$B_p(H) = B_0 \left( \frac{d + H}{d} \right)^{-2} = \left( \frac{B_0}{\sqrt{2}} \right), \quad (7)$$

which yields the relationship,

$$H = (2^{1/4} - 1) d \approx 0.189 d. \quad (8)$$

Note that the magnetic field  $B_p(H)$  drops over this height range  $H$  from  $B_0$  by a factor of  $B_0/\sqrt{2}$ , while the corresponding magnetic energy drops by a factor of  $E_{p,0}/2$  (Fig. 2), yielding an adequate approximation of the magnetized

flare volume  $V = AH$ , which contains to first order the same potential energy  $E_p$  as the exact volume integration defined in Eq. (2).

Now we need to estimate the depth  $d$  of the buried magnetic charges. The depth  $d$  is approximately equal to the sunspot radius  $r$ , at least for the largest magnetic charge in an active region (Aschwanden and Sandmann 2010), as we derive in the following. The radial magnetic field component is given by the square law,  $B_r = B_0(d/\rho)^{-2}$ , with  $\rho^2 = r^2 + d^2$  (see Fig. 1), which implies a line-of-sight component  $B_z$  of

$$B_z(r) = B_r(r) \cos \theta = B_p \left( \frac{d}{\rho} \right)^3 = \frac{B_p}{2} , \quad (9)$$

yielding a relationship between the depth  $d$  and the sunspot radius  $r$  (Fig. 1),

$$d = \frac{1}{\sqrt{2^{2/3} - 1}} \approx 1.30 r . \quad (10)$$

Besides these observables ( $B_p, L, r$ ) we have also a scaling factor for the flare area,  $q_A$ . In our original data analysis (Aschwanden et al. 2014a; Paper I) the flare area was measured where the magnetically dissipated energy  $E_{diss}(x, y, t)$  exceeds some threshold (i.e., the azimuthal magnetic field component  $B_{free} = B_\varphi \geq 100$  G), yielding a cumulative flare area  $A_{free}$  that monotonically grows during the flare duration. Generally, we expect the (nonpotential, potential, free energy, and dissipated) energy to scale in the following order:  $E_{np} \gtrsim E_p > E_{free} \gtrsim E_{diss}$  (see Table 1), and consequently we expect a similar order for the different area measures associated with these energies, i.e.,  $A_{np} \gtrsim A_p > A_{free} \gtrsim A_{diss}$  (see Table 1). The area  $A_p$  of the potential energy (above some threshold) defines an empirical area correction factor  $q_A$  relative to the (measured) free energy area  $A_{free}$ ,

$$q_A = \frac{A_p}{A_{free}} . \quad (11)$$

We can determine this factor empirically from the ratio of the theoretically predicted potential field area  $A_p$  and the observed values from the areas  $A_{free}$  (measured in Paper I), amounting to  $q_A \approx 6$  in our models (Fig. 3).

Finally, inserting the expressions for the flare volume  $V$  (Eq. 5), the flare area  $A$  (Eq. 6), the depth  $d$  (Eq. 10), and the magnetic field strength  $B_p$  (Eq. 4) of the largest sunspot, we obtain the following scaling law for the potential field energy  $E_p$ ,

$$E_p = \frac{(2^{1/4} - 1)}{8\pi\sqrt{2^{2/3} - 1}} q_A B_p^2 L^2 r \approx 0.010 q_A B_p^2 L^2 r . \quad (12)$$

We can now compare the observed potential energies  $x = E_p^{obs}$ , as calculated from the data of 173 M- and X-class flares in Aschwanden et al. (2014a, Paper I) and Aschwanden et al. (2019a; Paper XI), with this theoretically predicted scaling law  $y = E_p^{theo}$  (Eq. 12), based on the observed values of magnetic field strength  $B_p$ , length scale  $L$ , and sunspot radius  $r$  of the 173 flare events. We show a scatter plot  $y(x)$  of these two quantities  $x$  and  $y$  in Fig. (3a), where we find a cross-correlation coefficient of  $CCC=0.69$ , a scaling factor of  $q_A = 6.28$ , and a slope of  $\alpha = 1.60$  for the linear regression fit of the logarithmic values, i.e.,  $\log(y) = const + \alpha \times \log(x)$ . Obviously, the theoretically derived scaling law (Eq. 12) does not match the observed values exactly (Fig. 3a).

In order to explore other related scaling laws, we test also models where one or two of the three parameters  $[B_p, L, r]$  (Eq. 12) are uncorrelated (for instance because of too large uncertainties in their measurements). These alternative choices lead to six variants of the scaling law for the potential field energy:

$$E_p = 0.01 \times q_A \begin{cases} B_p^2 L^2 r & \propto B_p^2 L^2 r & \text{Model 1a} \\ B_p^2 L^2 r_0 & \propto B_p^2 L^2 & \text{Model 1b} \\ B_p^2 L^2 r & \propto B_p^2 r & \text{Model 1c} \\ B_p^2 L^2 r_0 & \propto B_p^2 & \text{Model 1d} \\ B_{p0}^L L^2 r & \propto L^2 r & \text{Model 1e} \\ B_{p0}^2 L^2 r_0 & \propto L^2 & \text{Model 1f} \end{cases} , \quad (13)$$

We denote the uncorrelated parameters with the subscript '0', i.e.  $(B_{p0}, R_0, L_0, r_0)$ , for which we simply use the median values (Table 1) rather than the observed individual values. These modified scaling laws are still based on a physical

model, although with noisy variables, and thus are candidates of possibly valid scaling laws. We show the observed values  $E_p$  and the values predicted by the six scaling laws in Fig. 3 and in Table 2.

In order to assess the consistency between theoretical scaling laws and observed values we use two different criterions (Section 2.2): The cross-correlation coefficient CCC, and the linear regression slope  $\alpha$ , which in the case of a perfectly matching model should converge to unity, i.e., CCC=1.0 and  $\alpha = 1.0$ . Investigating the six trial models (Eq. 13), we find that all models show a significant cross-correlation coefficient (CCC=0.53-0.71) between the observed potential energies  $E_p$  (x-axis in Fig. 3) and the scaling laws  $E_p[B_p, L, r]$  (y-axis in Fig. 3). However, the linear regression fits do not have a slope of unity (in logarithmic space), as it is expected for a matching scaling law. In contrast we find slopes of  $\alpha = 0.54 - 1.60$  (Fig. 3 and Table 2), which indicate missing variables in the proposed scaling law or large uncertainties. The best-fitting case is model 1f (Fig. 3f) with a scaling law of  $E_p \propto L^2$ , yielding a slope of  $\alpha = 1.13$  and a cross-correlation coefficient of CCC=0.64 (Fig. 3f). The other related models have all good cross-correlation coefficients (CCC=0.53-0.71) but exhibit significant deviations from the ideal powerlaw slope ( $\alpha = 0.54 - 1.60$ ), which indicate the various biases that occur from uncorrelated (noisy) parameters  $[B_p, L, r]$ , or unknown missing parameters in the tested scaling laws (Eq. 13).

We learn from testing six trial scaling laws (Eq. 13) of the potential field energy  $E_p$  that the most relevant parameter is the magnetic length scale  $L$  (or the corresponding magnetic flare area  $A = L^2$ ), while the (peak) magnetic field strength  $B_p$  and sunspot radius  $r$  have a too small parameter range or are too noisy to impact the scaling law. Inserting the constant  $q_A = 6.3$  (Fig. 3f) and median values  $B_{p0} = 2000$  G and  $r = 4.3$  Mm (Table 1) into Eq. (12) we obtain then the best-fitting following scaling law (Model 1f),

$$E_p \approx 0.010 q_A B_p^2 L^2 r \approx 1.15 \times 10^{33} \left( \frac{L}{33 \text{ Mm}} \right)^2 \text{ [erg]} , \quad (14)$$

The benefit of this result is that the potential field energy can be estimated from the magnetic length scale  $L$  alone, without the necessity of measuring the peak magnetic field value  $B_p$  or the sunspot radius  $r$ . In this study, the magnetic area  $A = L^2$  is defined by the cumulative flare area where the free energy  $E_{free}(x, y, t)$  exceeds a threshold of the azimuthal magnetic field component, i.e.,  $B_{free} = B_\varphi \geq 100$  G.

### 3.2. Scaling Law of Helical Twisting

Many physical models of flares employ untwisting of stressed magnetic fields as a primary trigger of a flare event. In the simplest version, a potential field  $B_p$  becomes helically twisted in the preflare phase, up to a maximum twist that can be quantified with a non-potential field  $B_{np}$ , before it becomes unstable, e.g. due to the kink instability or torus instability, and consequently releases or dissipates a part  $E_{diss}$  of the free energy  $E_{free}$ ,

$$E_{diss} \lesssim E_{free} = E_{np} - E_p . \quad (15)$$

Because of the quadratic dependence of the magnetic energy on the magnetic field strength, i.e.,  $E \propto B^2/8\pi$ , we have a Pythagorean relationship between the three magnetic field components  $[B_{np}, B_p, B_{free}]$ , namely

$$B_{free}^2 = B_{np}^2 - B_p^2 . \quad (16)$$

which also provides a vector equation for the directions of the magnetic field components,

$$\mathbf{B}_{free} = \mathbf{B}_{np} - \mathbf{B}_p . \quad (17)$$

For the case of a helically twisted field, which can most conveniently be expressed with spherical coordinates  $(r, \varphi, \theta)$ , the potential field component is aligned with the radial field  $B_r$ , and the field component associated with the free energy contains the azimuthal twist  $B_\varphi$ , which is perpendicular to the radial component (by applying the Pythagorean relationship). The helical twist involves a partial rotation of a cylindrical flux tube around its symmetry axis, which can be expressed by the twist angle  $\mu$  relative to the untwisted potential field,

$$\tan \mu = \left( \frac{B_\varphi}{B_p} \right) = \left( \frac{E_{free}}{E_p} \right)^{1/2} = \left( 2\pi N_{twist} \frac{R}{L} \right) , \quad (18)$$

where  $N_{twist}$  is the number of full twisting turns,  $R$  is the mean radius of a helically twisted flux tube, and  $L$  is the mean loop (or flux tube) length. Thus, we can formulate a scaling law for the free energy  $E_{free}$  as a function of the

observables  $[E_p, N_{twist}, L, R]$ ,

$$E_{free} = E_p \left( 2\pi N_{twist} \frac{R}{L} \right)^2. \quad (19)$$

Inserting the scaling of the potential energy  $E_p$  (Eq. 12) into this expression (Eq. 19) we obtain a scaling law as a function of the observables  $[B_p, R, r]$ , which does not depend on the mean loop length  $L$ ,

$$E_{free} = 0.010 q_A (2\pi N_{twist})^2 B_p^2 R^2 r \approx 0.010 q_A B_p^2 R^2 r. \quad (20)$$

We apply this scaling law of the free energy  $E_{free}$  to the observed data and measured values  $[B_p, R, r]$ , in Fig. 4. The number of full turn twists has been found to have a mean value of  $N_{twist} \approx 0.15$  in an earlier study (Aschwanden 2020). We test six models of scaling laws by comparing with the observed free energy  $E_{free}$  (Fig. 4),

$$E_{free} = 0.010 q_A (2\pi N_{twist})^2 \begin{cases} B_p^2 R^2 r & \propto B_p^2 R^2 r \quad \text{Model 2a} \\ B_p^2 R^2 r_0 & \propto B_p^2 R^2 \quad \text{Model 2b} \\ B_p^2 R_0^2 r & \propto B_p^2 r \quad \text{Model 2c} \\ B_{p0}^2 R^2 r & \propto R^2 r \quad \text{Model 2d} \\ B_{p0}^2 R^2 r_0 & \propto R^2 \quad \text{Model 2e} \\ B_{p0}^2 R_0^2 r & \propto r \quad \text{Model 2f} \end{cases}. \quad (21)$$

The 6 cases shown in Fig. 4 exhibit which parameters are correlated and which are uncorrelated in the scaling law. The correlation of the scaling law  $E_{free} \propto B_p^2 R^2 r$  has a high cross-correlation coefficient (CCC=0.89; Fig. 4a), but produces a too steep slope ( $\alpha = 1.31$ ) of the linear regression fit. Eliminating the sunspot radius  $r$  yields still a good correlation for the reduced scaling law  $E_{free} \propto B_p^2 R^2$  (CCC=0.90; Fig. 4b), while eliminating the helical twisting radius  $R$  destroys the correlation for the reduced scaling law  $E_{free} \propto B_p^2 r$  (CCC=0.48; Fig. 4c). Eliminating the potential field  $B_p$  (Figs. 4d, 4e, 4f) yields similar results as by including this parameter (Figs. 4a, 4b, 4c), most likely because of the small parameter range of  $B_p$ . The best-matching fit occurs for the scaling law that contains the helical twisting radius  $R$  only, i.e.,  $E_{free} \propto R^2$ , with a cross-correlation coefficient of CCC=0.87 and slope  $\alpha = 1.1$  (Fig. 4e), which can be formulated as,

$$E_{free} \approx 0.010 q_A (2\pi N_{twist})^2 B_{p0}^2 R^2 r_0^2 \approx 6.4 \times 10^{31} \left( \frac{R}{7.8 \text{ Mm}} \right)^2 \text{ [erg]}. \quad (22)$$

The benefit of this result is that the free energy, which is generally close to the magnetically dissipated flare energy,  $E_{diss} \lesssim E_{free}$ , can be estimated from the helical twisting radius  $R$  alone (for instance by using the VCA-NLFFF code), without the necessity of measuring the peak magnetic field value  $B_p$  or the sunspot radius  $r$ . Apparently the observables  $B_p$  and  $r$  have too small a range for this data sample (of M- and X-class flares) to affect the generalized scaling law (Eq. 20) for helical untwisting during flares.

### 3.3. Scaling Law for Petschek-Type Magnetic Reconnection

A common configuration of magnetic reconnection processes in the lower solar corona involves the interaction between two (more or less) vertical field lines with opposite magnetic polarity, which exchange their connectivity. The geometry is characterized by an X-point, where horizontal plasma inflows with low speed is transported through the diffusion region and produces accelerated Alfvénic outflows in downward and upward direction (Fig. 6). We can characterize the diffusion region with a typical length scale  $L$  in horizontal, vertical, and line-of-sight direction. Assuming that sideward inflows last for the duration  $\tau_{flare}$  of a flare, starting at a distance of  $L/2$  from the center of the X-point (Fig. 6, left panel), we can estimate the inflow velocity as,

$$v_1 = \frac{L/2}{\tau_{flare}}, \quad (23)$$

which has mean value of  $v_1 = 22 \text{ km s}^{-1}$ , according to our measurements of  $L = 40 \pm 25 \text{ Mm}$  for the magnetic length scale and  $\tau_{flare} = 900 \text{ s}$  for the flare duration (Table 2). The magnetic energy  $E_{diss}$  dissipated during a flare can be expressed by the magnetic energy that is processed through the diffusion region with a volume of  $V = L^3$  and an

inflow rate of  $dV/dt = L^2 v_1$ , which yields with Eq. (23), with consideration of doubling the half flare volume on either side of the X-point,

$$E_{diss} = \int \left( \frac{dE}{dt} \right) dt = 2 \left( \frac{B_{free}^2}{8\pi} \right) \frac{dV}{dt} \tau_{flare} = \left( \frac{B_{free}^2}{4\pi} \right) L^2 v_1 \tau_{flare} = \left( \frac{B_{free}^2}{8\pi} \right) L^3 , \quad (24)$$

where  $B_{free}$  is the magnetic field strength associated with the free energy. From the definition of the free energy  $E_{free}$  in terms of the difference between the nonpotential  $E_{np}$  and the potential energy  $E_p$  (Eq. 15), we can determine the mean value of  $B_{free}$  from their (observed and measured) energy ratio,

$$B_{free} = B_p \left( \frac{E_{free}}{E_p} \right)^{1/2} . \quad (25)$$

Therefore, the magnetic reconnection scenario of Petschek predicts a scaling law of  $E_{diss} \propto B_{free}^2 L^3$  (Eq. 24) that is based on the observables  $[B_{free}, L]$ .

We show this scaling law in Fig. 5a, compared with the observed values of  $E_{diss}$ , exhibiting a strong cross-correlation coefficient of CCC=0.87 for the dissipated energy  $E_{diss}$  (Fig. 5a). However, the slope of the linear regression fit, which should be near unity for a matching scaling law, deviates by a value of  $\alpha = 1.51$  (Figs. 5a).

We explore six different geometries as variants of the tested scaling laws:

$$E_{diss} = q_c \begin{cases} B_{free}^2 L^3 & \propto B_{free}^2 L^3 \quad \text{Model 3a} \\ B_{free}^2 L^2 L_0 & \propto B_{free}^2 L^2 \quad \text{Model 3b} \\ B_{free}^2 L L_0^2 & \propto B_{free}^2 L^1 \quad \text{Model 3c} \\ B_{free,0}^2 L^3 & \propto L^3 \quad \text{Model 3d} \\ B_{free,0}^2 L^2 L_0 & \propto L^2 \quad \text{Model 3e} \\ B_{free,0}^2 L L_0^2 & \propto L^1 \quad \text{Model 3f} \end{cases} . \quad (26)$$

These six models include cubic volume flare geometries  $E_{diss} \propto L^3$  (Figs. 5a, 5d); square area flare geometries  $E_{diss} \propto L^2$  (Figs. 5b, 5e); and linear flare geometries  $E_{diss} \propto L$  (Figs. 5c, 5f). In other words, a linear geometry involves scaling with the length scale  $L$  in horizontal direction only (while the other sides have random lengths with a mean of  $L_0$  and are not correlated with  $L$ ); a square geometry involves scaling with the squared area  $L^2$  while the vertical side has a random length and is not correlated with  $L^2$ . From the six samples shown in Fig. 5 we see that the slope of the linear regression fits decreases with the degree of the geometric dimensions. We find a best fit for the linear model  $E_{diss} \propto B_{free}^2 L$ , with a cross-correlation coefficient of CCC=0.92 and a slope of  $\alpha = 0.95$  (Fig. 5c),

$$E_{diss} \approx q_C \frac{B_{free}^2 L L_0^2}{8\pi} \approx 1.1 \times 10^{32} \left( \frac{B_{free}}{450 \text{ G}} \right)^2 \left( \frac{L}{33 \text{ Mm}} \right) \text{ [erg]} , \quad (27)$$

Thus we conclude that the horizontal inflow of plasma into the reconnection region with speed  $v_1 = (L/2)\tau_{flare}$  along the horizontal x-direction  $L$  is the most dominant parameter for the scaling law of the dissipated energy, while the extent of the reconnection region in the line-of-sight z-direction and in the vertical y-direction is uncorrelated to the horizontal scale size  $L$ , and thus does not affect the scaling law of the Petschek-type magnetic reconnection model.

### 3.4. The Rosner-Tucker-Vaiana Scaling Law

The Rosner-Tucker-Vaiana (RTV) scaling law (Rosner et al. 1978) has originally been designed to quantify a steady-state solution of a coronal loop, where the volumetric heating rate is balanced by the conductive and radiative loss rate. In addition, the RTV scaling law has been successfully applied to solar flares also, which consist of loop assemblies with complex magnetic topologies and geometries. Although the dynamics of flare loop systems is certainly not quasi-stationary during a flare, there is a critical equilibrium point at the flare peak time where heating and (conductive and radiative) cooling are approximately in balance, while the pre-flare phase is dominated by heating, and the post-flare phase is dominated by cooling.

The analytical solution can be expressed by four physical variables: the loop length of the thermal plasma  $L_{th}$ , the maximum temperature  $T_{max}$ , the pressure  $p_0 = 2n_e k_B T_{max}$ , and the volumetric heating rate  $E_{H0}$ :

$$T_{max} \approx 1400(p_0 L_{th})^{1/3} , \quad (28)$$

$$E_{H0} \approx 0.98 \times 10^5 p_0^{7/6} L_{th}^{-5/6} = 0.95 \times 10^{-6} T_{max}^{7/2} L_{th}^{-2} . \quad (29)$$

An alternative formulation of the RTV law that contains the electron density  $n_e$ , emission measure  $EM$ , and multi-thermal energy  $E_{th}$  has been given in Aschwanden and Shimizu (2013) and in Aschwanden et al. 2015 (Paper II),

$$T_{RTV} = 1.1 \times 10^{-3} n_e^{1/2} L_{th}^{1/2} , \quad (30)$$

$$n_{RTV} = 8.4 \times 10^5 T_e^2 L_{th}^{-1} , \quad (31)$$

$$L_{RTV} = 8.4 \times 10^5 T_e^2 n_e^{-1} , \quad (32)$$

$$EM_{RTV} = 1.5 \times 10^{12} T_e^4 L_{th} , \quad (33)$$

$$E_{th,RTV} = 7.3 \times 10^{-10} T_e^3 L_{th}^2 . \quad (34)$$

We are testing now these five scaling law relationships separately in Fig. 7. Most of them have a high cross-correlation coefficient in the range of CCC=0.56-0.92, which corroborates the validity of the RTV scaling laws. Three of these five relationships exhibit even a matching linear regression slope of  $\alpha \lesssim 1.1$ . The best match is found for the RTV scaling law of the thermal energy  $E_{th,RTV} \propto T_e^3 L_{th}^2$ , with CCC=0.92 and  $\alpha = 1.00$  (Fig. 7e).

The five scaling parameters are five different formulations of the same RTV scaling law and thus are redundant, but they demonstrate that the accuracy in the determination of a scaling law improves with larger parameter ranges: the thermal energy has the largest range of about three orders of magnitude and exhibits the highest correlation coefficient (CCC=0.92) and a perfect slope of  $\alpha = 1.00$  (Fig. 7e), while the temperature has a range of less than one order of magnitude, with CCC=0.77 and  $\alpha = 0.63$  (Fig. 7a). In the overall, our assessment of significant cross-correlation coefficients (CCC>0.5) and matching slopes ( $\alpha \lesssim 1.1$ ) in three cases corroborates the existence and validity of the RTV scaling law in the application to solar flares. The uncertainty of measurements that restrict the accuracy of detected scaling laws is expected to improve with larger parameter ranges (e.g., by including GOES C-class events, besides the M- and X-class flares sampled here).

### 3.5. Shibata-Yokoyama Scaling Laws

Assuming that the energy release in solar or stellar flares is dominated by magnetic reconnection and conductive energy loss, “universal scaling laws” were derived that roughly agree with MHD simulations (Yokoyama and Shibata 1998; Shibata and Yokoyama 1999, 2002). The analytical derivation of these scaling laws is based on four assumptions: (i) The flare temperature at the loop apex is balanced by the conduction cooling rate and the volumetric heating rate ( $Q = d/ds(\kappa_0 T^{5/2} dT/ds) \approx (2/7) \kappa_0 T_e^{7/2} / L_{th}^2$ ), with the Spitzer conductivity constant  $\kappa_0$ , yielding a flare loop apex temperature of,

$$T_e \approx \left( \frac{2Q L_{th}^2}{\kappa_0} \right)^{2/7} , \quad (35)$$

(ii) the heating rate  $Q$  is given by the reconnection rate in Petschek’s theory (with inflow velocity  $v_{in}$ , outflow (Alfvénic) velocity  $v_A$ , and shock inclination angle  $\sin \theta = v_{in}/v_A$  equivalent to the Alfvénic Mach number  $M_A = v_{in}/v_A$ ,

$$Q = \left( \frac{B^2}{4\pi} \right) \left( \frac{v_{in}}{v_A} \right) \left( \frac{1}{\sin \theta} \right) \approx \left( \frac{B^2}{4\pi} \right) \left( \frac{v_A}{L_{th}} \right) , \quad (36)$$

(iii) the upper limit of the gas pressure is given by the magnetic energy density,

$$p_{th} = 2n_e k_B T_e = p_m = \left( \frac{B^2}{8\pi} \right) , \quad (37)$$

and (iv) the volume of the heated flare plasma is approximated by a cubic geometry with total emission measure  $EM$  of,

$$EM \approx n_e^2 L_{th}^3 . \quad (38)$$

Using these four assumptions, four scaling laws can be expressed explicitly by the parameters  $T_e$ ,  $n_e$ ,  $EM$ ,  $B$ , and  $L_{th}$ ,

$$T_e = 3 \times 10^7 \left( \frac{B}{50 \text{ G}} \right)^{6/7} \left( \frac{n_e}{10^9 \text{ cm}^{-3}} \right)^{-1/7} \left( \frac{L_{th}}{10^9 \text{ cm}} \right)^{2/7} [\text{K}] , \quad (39)$$

$$EM = 10^{48} \left( \frac{B}{50 \text{ G}} \right)^{-5} \left( \frac{n_e}{10^9 \text{ cm}^{-3}} \right)^{3/2} \left( \frac{T_e}{10^7 \text{ K}} \right)^{17/2} [\text{cm}^{-3}] , \quad (40)$$

$$B = 50 \left( \frac{EM}{10^{48} \text{ cm}^{-3}} \right)^{-1/5} \left( \frac{n_e}{10^9 \text{ cm}^{-3}} \right)^{3/10} \left( \frac{T_e}{10^7 \text{ K}} \right)^{8/3} [\text{G}] , \quad (41)$$

$$L_{th} = 10^9 \left( \frac{EM}{10^{48} \text{ cm}^{-3}} \right)^{1/5} \left( \frac{n_e}{10^9 \text{ cm}^{-3}} \right)^{-2/5} \left( \frac{T_e}{10^7 \text{ K}} \right)^{-8/5} [\text{cm}] . \quad (42)$$

We are testing now these four variants of the Shibata-Yokoyama scaling laws in Fig. 8, using our SDO-based measurements of  $T_e \approx T_w$ ,  $B \approx B_{np}$ ,  $n_e \approx n_e^{inflow}$ ,  $L_{th}$ , and  $EM$ . The best-fitting model is  $L_{th} \propto EM^{1/5} n_e^{-2/5} T^{-8/5}$ , with a cross-correlation coefficient of CCC=0.68 and a linear regression slope of  $\alpha = 0.97$  (Fig. 8c). The other fitting model is  $EM \propto L_{th}^{5/3} n^{2/3} T^{8/3}$  with a correlation of CCC=0.76 and a slope of  $\alpha = 1.05$  (Fig. 8d). The other variants indicate that the relative range of parameter variations is extremely narrow for the scaling laws of the temperature  $T_e$  and the magnetic field  $B_{np}$  (Fig. 8b), which implies a large uncertainty in the linear regression slope of these two parameters, in contrast to the other two relationships of the emission measure  $EM$  and length scale  $L_{th}$ . Nevertheless, these tests mostly corroborate the validity of the Shibata-Yokoyama scaling laws, given the large uncertainties in the cross-correlation coefficients CCC and resulting linear regression fits of those parameters with narrow distributions.

These equations that enable us to test the EM-T relationship, derived in Shibata and Yokoyama (1999), have been referred to as the *pressure balance scaling law*, where the parameters  $[T_e, EM, B, L_{th}]$  are explicitly expressed as a function of the parameters  $[B, L_{th}, n_e, T_e]$ . An alternative formulation of the parameters has been derived in Shibata and Yokoyama (2002), so that the parameters  $[EM, B, L_{th}]$  are expressed as a function of the parameters  $[L_{th}, n_e, T_e]$ :

$$EM = 10^{48} \left( \frac{L_{th}}{10^9 \text{ cm}} \right)^{5/3} \left( \frac{n_e}{10^9 \text{ cm}^{-3}} \right)^{2/3} \left( \frac{T_e}{10^7 \text{ K}} \right)^{8/3} [\text{cm}^{-3}] , \quad (43)$$

$$B = 50 \left( \frac{EM}{10^{48} \text{ cm}^{-3}} \right)^{-1/5} \left( \frac{n_e}{10^9 \text{ cm}^{-3}} \right)^{3/10} \left( \frac{T_e}{10^7 \text{ K}} \right)^{17/10} [\text{G}] , \quad (44)$$

$$L_{th} = 10^9 \left( \frac{EM}{10^{48} \text{ cm}^{-3}} \right)^{3/5} \left( \frac{n_e}{10^9 \text{ cm}^{-3}} \right)^{-2/5} \left( \frac{T_e}{10^7 \text{ K}} \right)^{-8/5} [\text{cm}] . \quad (45)$$

We subject the two sets of Shibata-Yokoyama scaling laws to consistency tests with observational data. In Fig. 8 we show the correlation plots for the pressure balance scaling law (Figs. 8a, 8b, 8d, 8e), juxtaposed to the alternative Shibata-Yokoyama scaling laws (Figs. 8c and 8f). The scaling law of the emission measure  $EM(L_{th}, n_e, T_e)$  (Eq. 43) with CCC=0.76 and  $\alpha=1.05$  (Fig. 8d) is found to be fully consistent with the data (i.e., 173 GOES M- and X-class flares). Also the Shibata-Yokoyama pressure balance scaling law for the mean flare loop length scale  $L_{th}(EM, n_e, T_e)$  (Eq. 45), with CCC=0.68 and  $\alpha=0.97$  (Fig. 8c) is fully consistent with the data. However, the Shibata-Yokoyama scaling laws for the magnetic field  $B[EM, n_e T_e]$  (Eq. 44 and Figs. 8b and 8e), as well as the temperature  $T_e[B, n_e, L_{th}]$  (Eq. 39) are not consistent with the data. The reason for this inconsistency is most likely the very narrow range of values  $B$  and  $T_e$  that is an idiosyncracy of our data set containing the largest flares only (GOES M- and X-class). We expect that this selection bias can be overcome by extending the tested data sets to smaller (C-class and less) flares.

## 4. DISCUSSION

### 4.1. Coronal Heating Scaling Laws

Since heating of coronal plasma occurs both in non-flaring Quiet Sun regions as well as in flaring active regions, we comment on both processes in our discussion.

The most extensive compilation of scaling laws related to coronal heating has been presented in the pioneering study of Mandrini et al. (2000), entailing a total of 22 models, grouped into stressing (DC) and wave (AC) models. These power laws have the form of  $E_{heat} \propto B^\beta L^\lambda v^\gamma \dots$ , where  $E_{heat}$  is the heating rate,  $B$  is the mean magnetic field,  $L$  is a length scale, and  $v$  is a transverse velocity at the footpoints of coronal (magnetic) loops. The authors find that the mean magnetic field  $B$  scales with the length  $L$  of a magnetic field line by the relationship  $\log(B) = c_1 + c_2 \log L + c_3 / 2 \log(L^2 + S^2)$ , which can be approximated by a double power law, with different slopes for the near-field and far-field (magnetic) regime, but cannot be represented by a single power law relationship  $B \propto L^\delta$ . Nevertheless, reducing the data set to loops with intermediate lengths and combining it with a heating rate of  $E_{heat} \propto L^{-2}$  (Klimchuk and Porter 1995), a universal scaling law of  $B \propto L^{-0.88 \pm 0.3} \propto L^{-1}$  has been postulated, from which it was concluded that DC models are more consistent with observations than AC models (Mandrini et al. 2000). In contrast to this result of  $B \propto L^{-1}$ , one would expect that a potential field drops off with the square-distance law  $B \propto L^{-2}$  (Eq. 3), at least for field lines that originate at the strongest magnetic field location of an active region, which is generally dominated by the leading sunspot. Furthermore, a scaling law of the heating rate should primarily include the regions with the strongest magnetic fields, rather than magnetic field lines with intermediate lengths, as employed in the study of Mandrini et al. (2000).

A novel approach to identify coronal heating mechanisms has been presented by Schrijver et al. (2004), by simulating the full-Sun corona with an ensemble of 50,000 hydrostatic loops, subject to a constant heating rate with the parameterization  $F_{heat} \propto B^\beta L^\lambda$ , for which a best-fit scaling law of  $F_{heat} \propto B^{1.0 \pm 0.3} L^{-1.0 \pm 0.5}$  was found. Since this formulation using the Poynting flux  $F_{heat}$  (in units of  $\text{erg cm}^{-2} \text{ s}^{-1}$ ) relates to the volumetric heating rate  $\varepsilon_{heat} \propto F_{heat}/L$  (in units of  $\text{erg cm}^{-3} \text{ s}^{-1}$ ), we would expect a scaling law of  $\varepsilon_{heat} \propto B^1 L^{-2}$  for the volumetric heating rate, and a scaling law of  $E_{heat} \propto \varepsilon_{heat} L^3 \tau_{dur} \propto B^1 L^1 \tau_{dur}$  (in units of erg) for the total dissipated energy. This hypothetical scaling law is in marked contrast to other heating models or flare models, which all have the basic relationship of magnetic energies in terms of  $E_{magn} \propto B^2 L^3$  (Eqs. 4, 12, 20, 24) in physical units of  $\text{erg} = \text{G}^2 \text{ cm}^3$ . Schrijver et al. (2004) point out that their result is consistent with the allowed models in the study of Mandrini et al. (2000), but the dependence of the heating flux density  $F_{heat}$  with  $B/L$  is also consistent with the study by Démoulin et al. (2003), although a volumetric heating rate of  $\varepsilon_{heat} \propto B^2$  has been claimed therein. Note that all magnetic scaling models used here are based on the scaling of  $E_{magn} \propto B^2$ . Regarding self-consistency tests, the simulations of Schrijver et al. (2004) do show the correlation between the observed soft X-ray fluxes and the simulated fluxes based on the scaling law of  $B/L$ , but do not demonstrate whether there is a significant correlation between the observed ( $F_{heat}$ ) and the simulated heating rate ( $\propto B/L$ ).

### 4.2. Helical Twist Scaling Laws

Free (magnetic) energy can be stored by helical twisting of magnetic flux tubes. This twist can be measured in terms of the number of full turns, where the free energy monotonically increases with the twist angle (Eq. 18), up to a maximum rotation angle that triggers the kink instability, which occurs after about one full turn, i.e.,  $N_{twist} \approx 1.0 - 1.5$  (Hood and Priest 1979, 1981; Török and Kliem 2003; Kliem et al. 2010). From our derivation of a twist-related scaling law (Section 2.2) we found that the free energy depends mostly on the twisted flux tube radius  $R$  (Eq. 22), but not significantly on other parameters, such as the magnetic field strength  $B_p$ , the sunspot radius  $r$ , or the loop length  $L$ . The flux tube radius  $R$  of helical twist corresponds to the distance of detected twisted field lines from the symmetry axis of the underlying potential field, which amounts here to  $R = 12 \pm 12 \text{ Mm}$  (Table 1), which is generally outside of the sunspot radius of  $r \approx 4.5 \pm 1.1 \text{ Mm}$ .

How is the helical twist measured in the solar corona? Fortunately, the VCA-NLFFF code parameterizes the magnetic field into three orthogonal components, where the azimuthal component  $B_{free} = B_\varphi$  contains all information about the helical twist relative to the (untwisted) potential field component. This way we obtained in a previous statistical study (Aschwanden 2019c) a twist number (or Gauss linkage number) of  $N_{twist} = 0.14 \pm 0.03$ , with an absolute upper limit of  $N_{twist} \lesssim 0.5$ , which is about a factor of two below the kink instability. This somewhat lower (than expected) value may indicate that no force-free field solution exists in that regime of  $N_{twist} \approx 0.5 - 1.0$ .

Agreement has been found between magnetic helicity estimations and a twist number method, as calculated with the Berger-Prior formula, which is supposed to be suitable for arbitrary geometry and both force-free and non-force-free models (Guo et al. 2017). The twist number method has been applied to MHD simulations from a NLFFF code, over a range of  $N_{twist} = 0.02 - 0.61$  (Guo et al. 2017) that is similar to the results from our VCA-NLFFF code, i.e.,  $N_{twist} \lesssim 0.5$  (Aschwanden 2019c).

#### 4.3. Magnetic Reconnection Scaling Laws

Soft X-ray and EUV emission of solar flares, observed during the Yohkoh era, provided strong evidence for the existence of magnetic reconnection processes. The theoretical modeling focused first on the Sweet-Parker current sheet model (Sweet 1958; Parker 1963, 1988), which was found to be too slow to account for the impulsive flare phase, while a more realistic concept was initiated with the Petschek model (Petschek 1964; Aschwanden 2020). A salient feature of the Petschek model is the smaller size of the X-type current sheets, which allows for a slow horizontal inflow (with speed  $v_{in} \approx 20 \text{ km s}^{-1}$ ) and fast vertical Alfvénic outflows (with a typical speed of  $v_A \approx 2000 \text{ km s}^{-1}$ ), which corresponds to an Alfvénic Mach number of  $M_A = v_{in}/v_A \approx 0.01$ , consistent with the expected high Lundquist number of  $R_m \approx 10^8 - 10^{12}$  in the solar corona. The related magnetic reconnection rate  $dV/dt \propto L^2 v_{in}$  with  $v_{in} = (L/2)/\tau_{flare}$  provides the most basic expression for the dissipated magnetic energy in a flare, i.e.,  $E_{diss} \propto B_{free}^2 V$  (Eq. 24), where  $V$  approximates the geometry of the diffusive reconnection region with a simple (self-similar) cube,  $V \approx L^3$ . Our fitting procedure of the suspected scaling law  $E_{diss} \propto B_{free}^2 L^3$ , however, does not match the observations (Fig. 5a), while the one-dimensional geometry  $E_{diss} \propto B_{free}^2 L \times L_0^2$  fits the observations with both criteria, the cross-correlation coefficient  $CCC \approx 1$  and the linear regression slope  $\alpha \approx 1$ , (Fig. 5c). The difference between the two volume scalings,  $V = L^3$  versus  $V = L L_0^2$ , where  $L_0$  is a constant, corresponding to the median value  $L_0 = median(L)$ , simply implies that the vertical ( $L_y$ ) and line-of-sight dimensions ( $L_z$ ) of the diffusive reconnection region are not correlated with the horizontal dimension ( $L = L_x$ ) (Fig. 6), allowing the volume of the diffusive reconnection region to possess any arbitrary rectangular geometry with dimensions  $V = L_x L_y L_z$ . The 1-D scaling  $E_{diss} \propto B_{free}^2 L$ , furthermore, requires a lower state of order than the 3-D scaling  $E_{diss} \propto B_{free}^2 L^3$ , and thus is preferable according to Ockham's razor.

Originally, Yokoyama and Shibata (1998) tested a Petschek-type scaling law with MHD simulations, assuming that the scaling law obeys the relationship  $T_e \propto B^{6/7}$  (Eq. 39). A more complete derivation of Petschek-type flare scaling laws was presented in Shibata and Yokoyama (1999), based on the assumptions that flare heating is balanced by the conductive cooling rate, and that the gas pressure is limited by the magnetic energy density (Eq. 35-36). Quantitative evidence of the Yokoyama-Shibata “universal scaling law” has been demonstrated by the fact that Yohkoh-observed solar flares are bracketed in the emission measure-temperature  $EM - T$  diagram by solar microflares and stellar giant flares (Fig. 1 in Shibata and Yokoyama 1999). However, this matching of the the  $EM - T$  diagram does not fully demonstrate a cross-correlation between the observed and theoretically predicted scaling laws. In this study we tested the Yokoyama-Shibata with 172 flare events observed with SDO and find that a good match for two of the four Shibata-Yokoyama relationships, i.e.,  $L \propto EM^{1/5} n_e^{-2/3} T^{-8/5}$  (Fig. 8c), and  $EM \propto L^{5/3} n_e^{2/3} T^{8/3}$  (Fig. 8d), while the two other scaling laws do not corroborate the expected scaling laws, most likely because the temperature  $T$  and magnetic field strength  $B$  exhibit a very narrow parameter range (see also standard deviations in Table 2). Hence, the parameter ranges have to be expanded by including smaller flares (of GOES C-class and below) to corroborate the validity of the Shibata-Yokoyama scaling law.

Shibata and Yokoyama (2002) generalized the observationally established emission measure-temperature relationship  $EM \propto T^4$  by combining different hydrostatic models, such as the thermal conduction-driven model (Eq. 35), the magnetic-thermal pressure balance model (Eq. 37), or the enthalpy-conduction balance model ( $5n_e k_B T C_s \approx \kappa_0 T^{7/2}/L$ ). Moreover, certain forbidden regions in the EM-T diagram have been identified, for instance when chromospheric evaporation sets in and the thermal pressure overcomes the magnetic pressure so that plasma confinement is not possible anymore, which violates the assumption of the gas pressure being an upper limit of the magnetic energy density (Eq. 37). We find that our self-consistency criteria ( $CCC \lesssim 1.0$  and  $\alpha \approx 1$ ) provide powerful tests to sort out which model is most consistent with the observed flare data.

#### 4.4. Thermal Flare Emission Scaling Laws

We tested and discussed the RTV scaling law previously in Paper II (see Fig. 7 therein). The Rosner-Tucker-Vaiana (RTV) law represents a generalization of the Shibata-Yokohama model on one side, based on the assumption that the heating rate  $E_{heat}$  is balanced by both the conductive  $E_{cond}$  and the radiative loss rate  $E_{rad}$ , i.e.,  $E_{heat} = E_{cond} + E_{rad}$ ,

while it is a reduction on the other side, by including thermal parameters only and ignoring magnetic parameters. Another special condition in the application of the RTV law is that the energy balance applies only to the peak time of the flare, where the heating rate dominates over the loss rates before the flare peak time (including the preflare phase), while conductive and radiative losses dominate the heating rate after the flare peak (fading into the post-flare phase). We find that our self-consistency tests with the flare data yield the best agreement for the thermal energy parameter,  $E_{th} \propto T_e^3 L_{th}^2$ , with CCC=0.92 and  $\alpha = 1.00$  (Fig. 7e). The other RTV parameters,  $[T_e, L_{th}, n_e, EM]$ , show all a significant correlation (CCC>0.56), but exhibit a deviation from the linear regression slope of  $\alpha = 1$ , most likely because of the narrow temperature range, since the temperature occurs in each of the five RTV scaling law formulations shown in Fig. 7 (Eqs. 30-33). In contrast, the thermal energy displays the largest parameter range of about 3 orders of magnitude ( $E_{th} \approx 10^{31} - 10^{44}$  erg, Fig. 7e). We learn from our analysis that it is of utmost importance to cover a large parameter range in the linear regression fits when testing scaling laws. Larger parameter ranges that include C-, M-, and X-class flares have been measured by Warmuth and Mann (2016a, 2016b), for comparisons of thermal and non-thermal flare parameters. However, since the occurrence frequency distributions of solar flare parameters typically follow a power law distribution  $N(x) \propto x^{-p}$  with a power law index of  $p \approx 1.8$  (Crosby et al. 1991), completely sampled parameter data sets become prohibitively large below the M- or C-class level. Fortunately, the testing of scaling laws does not require complete sampling in cross-correlation tests.

## 5. CONCLUSIONS

In this study we tested 30 variants of 5 basic physical scaling laws that describe different aspects of solar flares, which includes: (i) a scaling law of the potential-field energy, (ii) a scaling law for helical twisting, (iii) a scaling law for Petschek-type magnetic reconnection, (iv) the Rosner-Tucker-Vaiana scaling law, and (v) the Shibata-Yokoyama scaling law. We test the self-consistency of these theoretical scaling laws with observed parameters by requiring two conditions, a cross-correlation coefficient of CCC> 0.5 between the observed and theoretically predicted scaling laws, and a near-identical linear regression slope  $\alpha \approx 1$  for the observed and theoretical scaling laws. These two criteria are necessary but not sufficient conditions to verify the existence and validity of theoretical scaling laws, but are rarely performed in the literature. In the following we summarize the best-fit solutions and their underlying physical assumptions, using a data set of 172 GOES M- and X-class flare events.

1. The potential field energy  $E_p$  is a lower limit to any non-potential field, and is a near-constant (or at least a slowly-varying) parameter during a solar flare. This potential field energy can be estimated from the peak of the magnetic field  $B_p(x, y, z)$  in an active region with volume  $V = AH$ , the height range  $H \approx 0.2 d$  over which the potential field energy decreases by half, which relates to the depth  $d$  of buried magnetic charges and the sunspot radius  $r$  by  $d \approx 1.3 r$ , yielding to the scaling law  $E_p \propto B_p^2 L^2 r$  (Eq. 13). Since the peak magnetic field  $B_p$  and the sunspot radius  $r$  have a narrow range of their values (for the given M- and X-class flare data set), the scaling law is dominated by the (mean) magnetic length scale  $L$ , i.e.,  $E_p \propto L^2$ , fulfilling the data consistency criteria with CCC=0.64 and  $\alpha = 1.1$  (Fig. 4e).
2. An upper limit of the dissipated magnetic energy in a flare is the free energy,  $E_{diss} \lesssim E_{free} = E_{np} - E_p$ . If the dissipated magnetic energy is entirely due to untwisting of the helically twisted flare loops, a scaling law can be formulated as a function of the potential field energy  $E_p$ , the number of full turn twist  $N_{twist}$ , and the radius  $R$  and length  $L$  of helically twisted cyclinders, i.e.,  $E_{free} \propto E_p N_{twist}^2 (R/L)^2$  (Eq. 20), or by inserting the scaling law on the potential energy,  $E_{free} \propto B_p^2 R^2 r$  (Eq. 21). Consistency with data is obtained with CCC=0.87 and  $\alpha = 1.1$  (Fig. 4e).
3. The Petschek-type magnetic reconnection in the X-point of a magnetic diffusion region predicts, based on the high magnetic Lundquist number in the solar corona, subsonic horizontal inflows of plasma ( $v_{in} \approx 20 \text{ km s}^{-1}$ ) into the diffusion region and acceleration at the X-point to Alfvénic vertical outflows ( $v_A \approx 2000 \text{ km s}^{-1}$ ) (in upward and downward directions), which yields a scaling law of  $E_{diss} \propto B_{free}^2 L^3$  (Eq. 24). However, the scaling of a one-dimensional volume with  $V \propto L^1$  is found to be more consistent with the data than the 3-dimensional volume  $V \propto L^3$ , which implies that the vertical  $L_y$  and line-of-sight dimension  $L_z$  are not correlated to the horizontal dimension  $L_x$ , yielding a modified scaling law of  $E_{diss} \propto B_{free}^2 L$  (Eq. 26). Consistency with data is obtained with CCC=0.92 and  $\alpha = 0.95$  (Fig. 5c).
4. The Rosner-Tucker-Vaiana (RTV) model is based on the assumption that a constant volumetric heating rate is balanced by thermal conductive and radiative loss, at the peak time of the flare, while heating is dominant

before the flare peak, and conductive and radiative losses are dominant after the flare peak. This leads to an equilibrium solution of  $T_e \propto (p_0 L)^{1/3}$  for a single loop with length  $L_{th}$ , pressure  $p_0$ , and apex temperature  $T_e$ . We find that 3 formulations of the RTV law are consistent with the data, explicitly expressed for the length scale  $L_{th} \propto T_e^3 n_e^{-1}$  (Fig. 7b), for the emission measure  $EM \propto T_e^4 L_{th}$  (Fig. 7d), and for the thermal energy  $E_{th} \propto T_e^3 L_{th}^2$  (Fig. 7e). The predicted scaling laws for the temperature  $T_e$  and electron density  $n_e$  could not be retrieved due to their small parameter range (of M- and X-class flares).

5. The Shibata-Yokoyama scaling law is a combination of the Petschek-type and RTV scaling laws, based on four physical assumptions; (i) the flare temperature at the loop apex is balanced by the heating rate and the conductive cooling rate, (ii) the heating rate is given by the reconnection rate in Petschek's theory, (iii) the upper limit of the (thermal) gas pressure is given by the magnetic energy density, and (iv) the volume of the heated flare plasma is estimated from a cubic geometry  $V = L^3$  in the emission measure  $EM = n_e^2 L_{th}^3$ . Best fits and consistency with the data is obtained for the expression of the length scale,  $L_{th} \propto EM^{1/5} n_e^{-2/5} T_e^{-8/5}$  with CCC=0.68 and  $\alpha = 0.97$  (Fig. 8c), and for the expression of the emission measure,  $EM \propto L_{th}^{5/3} n_e^{2/3} T_e^{8/3}$  with CCC=0.76 and  $\alpha = 1.05$  (Fig. 8d).

These results corroborate the validity of flare scaling laws for the five types of investigated flare phenomena, in the sense that we found self-consistency with observational data. Our data set here is biased towards large flares (of GOES M- and X-class), for which the temperature range ( $T_e = 26 \pm 6$  MK) as well as the range of the peak magnetic field strength ( $B_{np} = 2100 \pm 400$  G) is relatively narrow, so that the scaling cannot be retrieved. On the other side, scaling laws expressed explicitly for energies, emission measures, and length scales have sufficiently large parameter ranges (2-3 orders of magnitude) to constrain their power law indexes of scaling laws.

In summary, the self-consistency between observables and theoretically predicted scaling laws reveals the success or failure of a well-posed physical flare model, while model-free fitting of power law indices in heuristic expressions  $X = a^\alpha b^\beta \dots$  rarely reveal an adequate physical model. For instance, the best-fit result  $F_{heat} \propto B^1 L^{-1}$  found in simulations of coronal heating by Schrijver et al. (2004) clashes with the result of  $F_{heat} \propto B^2$  by Démoulin et al. (2003), since neither their physical units nor their power law exponents can be reconciled. In other words, fitting a physical model is preferable over evaluating model-free scaling laws without an underlying physical model. For future progress we recommend to increase narrow parameter ranges (such as temperature, density, and magnetic field parameters) in order to optimize flare scaling law tests.

**Acknowledgements:** We acknowledge software support by Samuel Freeland, Greg Slater, and Mark Noga. Part of the work was supported by NASA contract NNG04EA00C of the SDO/AIA instrument and the NASA STEREO mission under NRL contract N00173-02-C-2035.

## REFERENCES

Altschuler, M.D. and Newkirk, G.Jr. 1969, *SoPh* 9, 131

Aschwanden, M.J., Kosugi, T., Hudson, H.S., Wills, M.J. and Schwartz, R.A. 1996, *ApJ* 470, 1198

Aschwanden, M.J. 2007, *AdSpR* 39, 1867

Aschwanden, M.J., Stern, R.A., and Güdel, M. 2008, *ApJ* 672, 659

Aschwanden, M.J. 2010, *SoPh* 262, 235

Aschwanden, M.J. and Sandman, A.W. 2010, *ApJSS* 140:723

Aschwanden, M.J. 2013, *SoPh* 287, 323

Aschwanden, M.J. and Shimizu, T. 2013, *ApJ* 776, 132

Aschwanden, M.J., Zhang, J., and Liu, K. 2013, *ApJ* 775:23

Aschwanden, M.J., Xu, Y., and Jing, J. 2014a, *ApJ* 797:50 (Paper I)

Aschwanden, M.J., Boerner, P., Ryan, D., Caspi, A., McTiernan, J.M., and Warren, H.P. 2015a, *ApJ* 802:53 (Paper II)

Aschwanden, M.J., Boerner, P., Caspi, A., McTiernan, J.M., Ryan, D., and Warren, H. 2015b, *SoPh* 290, 2733

Aschwanden, M.J. 2019a, *ApJ* 885:49 (Paper IX)

Aschwanden, M.J. 2019c, *ApJ* 874:131

Aschwanden, M.J. 2020, *ApJ* 895:134, (Paper X)

Crosby, N.B., Aschwanden, M.J., and Dennis, B.R. 1993, *SoPh* 143, 275

Démoulin, P., van Driel-Gesztelyi, L., Mandrini, C.H., Klimchuk, J.A., and Harra, L. 2003, *ApJ* 586, 592

Garcia, H.A. 1998, *ApJ* 504, 1051

Guo, Y., Pariat, E., Valori, G., Anfinogentov, S., Chen, F., Georgoulis, M.K., Liu, Y., Moraitis, K., Thalmann, J.K., and Yang, S. 2017, *ApJ* 840:40

Hood, A.W. and Priest, E. 1979, *SoPh* 64, 303

Hood, A.W. and Priest, E. 1981, *GApFD* 17, 297

Kahler, S.W. 2013, *ApJ* 769:35

Kliem, B., Linton, M., Török, T., and Karlicky, M. 2010, *SoPh* 266, 91

Klimchuk, J.A. and Porter, L.J. 1995, *Nature* 377, 131

Lemen, J.R., Title, A.M., Akin, D.J., et al. 2012, *SoPh* 275, 17

Mandrini, C.H., Demoulin, P., and Klimchuk, J.A. 2000, *ApJ* 530, 999.

Morales, L.F. and Charbonneau, P. 2008, *GRL* 35, 4108M

Namekata, K., Sakaue, T., Watanabe, K., Asai, A., and Shibata, K. 2017, *PASJ* 69, id.7

Parker, E.N. 1963, *ApJS*, 8, 177

Parker, E.N. 1988, *ApJ* 330, 474

Pesnell, W.D., Thompson, B.J., and Chamberlin, P.C. 2012, *SoPh* 275, 3

Petschek, H.E. 1964, in *Proc. AAS-NASA Symp., The Physics of Solar Flares*, ed. W.N. Hess (Washington, DC: NASA), 425

Pugh, C.E., Broomhall, A.M., and Nakariakov, V.M. 2019, *A&A* 624, A65

Priest, E.R. 1975, *SoPh* 43, 177

Rosner, R., Tucker, W.H., and Vaiana, G.S. 1978, *ApJ* 220, 643

Sakurai, J.I. 1982, *SoPh* 76, 301

Scherrer, P.H., Schou, J., Bush, R.J. 2012, *SoPh* 275, 207

Schmidt, H.U. 1964, *NASA SP* 50, (ed. W.N. Hess), Washington DC

Schrijver, C.J., Sandman, A.W., Aschwanden, M.J., and DeRosa, M.L. 2004, *ApJ* 615, 512

Shibata, K. and Yokoyama, T. 1999, *ApJ* 526, L49

Shibata, K. and Yokoyama, T. 2002, *ApJ* 577, 432

Sweet, P.A. 1958, in *IAU Symp. 6, Electromagnetic Phenomena in Cosmic Physics*, (ed. B. Lehnert (Cambridge: Cambridge Univ. Press), 123

Török, T. and Kliem, B. 2003, *A&A* 406, 1043

Vekstein, G. and Katsukawa, Y. 2000, *ApJ* 541, 1096

Warmuth, A. and Mann, G. 2016a, *A&A* 588, A115

Warmuth, A. and Mann, G. 2016b, *A&A* 588, A116

Wiegmann, T., Inhester, B., and Sakurai, T. 2006, *SoPh* 223, 215

Yamamoto, T.T., Shiota, D., Sakajiri, T., Akiyama, S., Isobe, H., and Shibata, K. 2002, ApJ 579, 45  
Yokoyama, T. and Shibata, K. 1998, ApJ 494, 113

**Table 1.** Observational parameters of  $N = 173$  M- and X-class flare events analyzed in Aschwanden, Xu, and Jing (2014).

	Minimum	Maximum	Mean	Median
Nonpotential magnetic energy $E_{np}[10^{30} \text{ erg}]$	86	4900	$1500 \pm 1060$	1150
Potential magnetic energy $E_p[10^{30} \text{ erg}]$	53	5300	$1400 \pm 961$	1050
Free energy $E_{free}[10^{30} \text{ erg}]$	2.0	950	$120 \pm 160$	64
Dissipated magnetic energy $E_{diss}[10^{30} \text{ erg}]$	4.0	15	$180 \pm 250$	110
Nonpotential field strength $B_{np}[G]$	970	3000	$2100 \pm 400$	2000
Potential field strength $B_p[G]$	330	3200	$2000 \pm 340$	2000
Free energy field strength $B_{free}[G]$	84	1300	$500 \pm 240$	450
Dissipated energy field strength $B_{diss}[G]$	140	1700	$640 \pm 280$	590
Magnetic length scale L[Mm]	13	240	$40 \pm 25$	33
Sunspot radius r[Mm]	1.4	9.1	$4.5 \pm 1.1$	4.3
Helical twisting radius R[Mm]	1.3	77	$12 \pm 12$	7.8
Depth of magnetic charges d[Mm]	1.8	12	$5.8 \pm 1.4$	5.6
Flare duration $\tau_{flare}$ [s]	290	15000	$1500 \pm 1800$	900
Thermal length scale $L_{th}$ [Mm]	10.8	288.9	$75.5 \pm 44.5$	65.0
Emission measure-weighted electron temperature $T_e$ [MK]	5.7	41.6	$25.5 \pm 5.6$	26.1
Mean flare electron density $n_e$ [ $10^{10} \text{ cm}^{-3}$ ]	2.0	58.9	$10.4 \pm 7.3$	8.5
Total thermal emission measure EM [ $10^{40} \text{ cm}^3$ ]	1.1	447.7	$35.9 \pm 51.2$	20.1
Total thermal energy $E_{th}$ [ $10^{30} \text{ erg}$ ]	5.2	$\approx 1000$	$582.0 \pm 1120.7$	237.2

**Table 2.** Scaling Relationships are listed for 30 variants of 6 scaling law models, specified by the scaling factor  $q_A$ , the cross-correlation coefficient CCC, and the linear regression slopes  $\alpha$ .

Model	Scaling Relationship	Factor $q_A$	Coefficient CCC	Slope $\alpha$
1a	$E_p \propto B_p^2 L^2 r$	6.3	0.69	1.60
1b	$E_p \propto B_p^2 L^2$	5.9	0.71	1.43
1c	$E_p \propto B_p^2 r$	6.0	0.53	0.74
1d	$E_p \propto B_p^2$	6.2	0.55	0.54
1e	$E_p \propto L^2 r$	6.4	0.64	1.28
1f	$E_p \propto L^2$	6.3	0.64	1.13
2a	$E_{free} \propto B_p^2 R^2 r$	6.9	0.89	1.31
2b	$E_{free} \propto B_p^2 R^2$	7.2	0.90	1.22
2c	$E_{free} \propto B_p^2 r$	6.7	0.48	0.43
2d	$E_{free} \propto R^2 r$	7.1	0.88	1.18
2e	$E_{free} \propto R^2$	7.0	0.87	1.11
2f	$E_{free} \propto r$	6.9	0.40	0.19
3a	$E_{diss} \propto B_{free}^2 L^3$	0.23	0.87	1.51
3b	$E_{diss} \propto B_{free}^2 L^2$	0.23	0.90	1.22
3c	$E_{diss} \propto B_{free}^2 L$	0.22	0.92	0.95
3d	$E_{diss} \propto L^3$	0.22	0.67	0.98
3e	$E_{diss} \propto L^2$	0.22	0.67	0.65
3f	$E_{diss} \propto L$	0.22	0.67	0.33
4a	$T_e \propto n_e^{1/2} L_{th}^2$	1.17	0.77	0.63
4b	$L_{th} \propto T_e^3 n_e^{-1}$	0.65	0.64	1.12
4c	$n_e \propto T_e^2 L_{th}^{-1}$	0.61	0.77	1.46
4d	$EM \propto T_e^4 L$	0.42	0.56	1.13
4e	$E_{th} \propto T_e^3 L_{th}^2$	0.67	0.92	1.00
5a	$T_e \propto B^{6/7} n_e^{-1/7} L_{th}^{2/7}$	0.03	-0.01	1.18
5b	$EM \propto L_{th}^{5/3} n_e^{2/3} T_e^{8/3}$	0.03	0.44	0.84
5c	$B_{np} \propto EM^{-1/5} n_e^{3/10} T_e^{8/3}$	1.29	0.14	3.73
5d	$L_{th} \propto EM^{1/5} n_e^{-2/5} T_e^{-8/5}$	19.55	0.68	0.97
6a	$EM \propto L_{th}^{5/3} n_e^{2/3} T_e^{8/3}$	0.03	0.76	1.05
6b	$B_{np} \propto EM^{-1/5} n_e^{3/10} T_e^{17/10}$	3.26	0.11	2.67
6c	$L_{th} \propto EM^{3/5} n_e^{-2/5} T_e^{-8/5}$	7.57	0.87	1.35

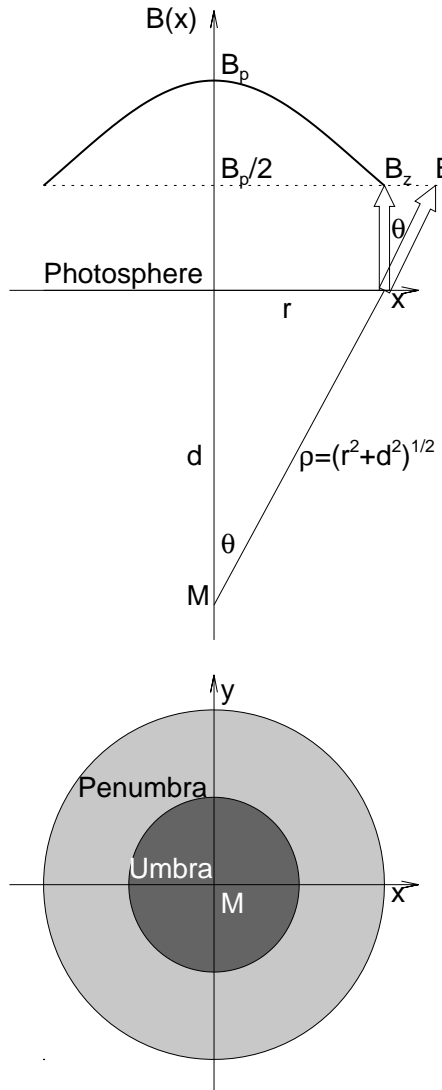


**Figure 1.** Schematic of sunspot parameters from a top view in the  $[x, y]$  plane, showing the umbra and penumbra (bottom panel), a side view with the location of the magnetic charge  $M$  at sunspot radius  $r$  and subphotospheric depth  $d$  (middle panel), and the potential field strength  $B(x)$  as a function of the radius  $x$ , with the sunspot radius  $r$  defined by the value of the half maximum peak  $B_p/2$  (top panel).  $B_r$  is the radial field component, and  $B_z$  is the line-of-sight component measured by the observer.

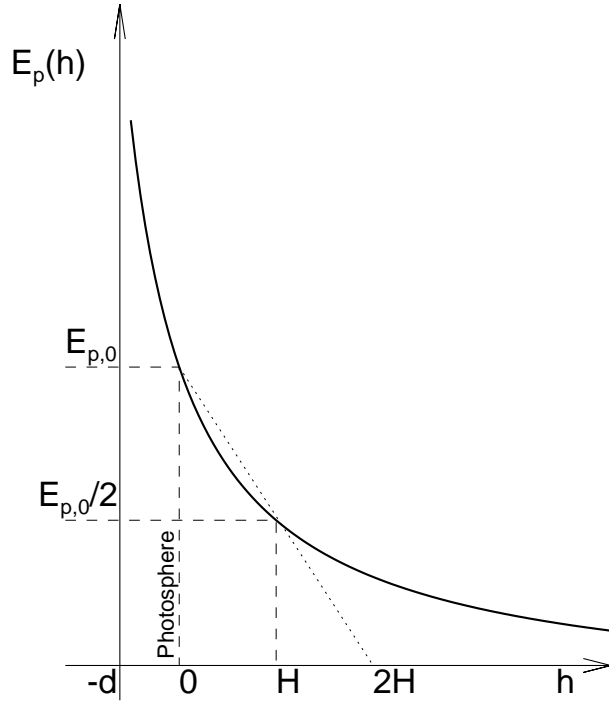


**Figure 2.** Schematic of height dependence of the magnetic field energy  $E_p(h)$ , with the magnetic charge located at a sub-photospheric depth  $h = -d$ , the photospheric height at  $h = 0$  with the peak energy value  $E_{p,0}$ , and the half peak value  $E_{p,0}/2$  at  $h = H$ .

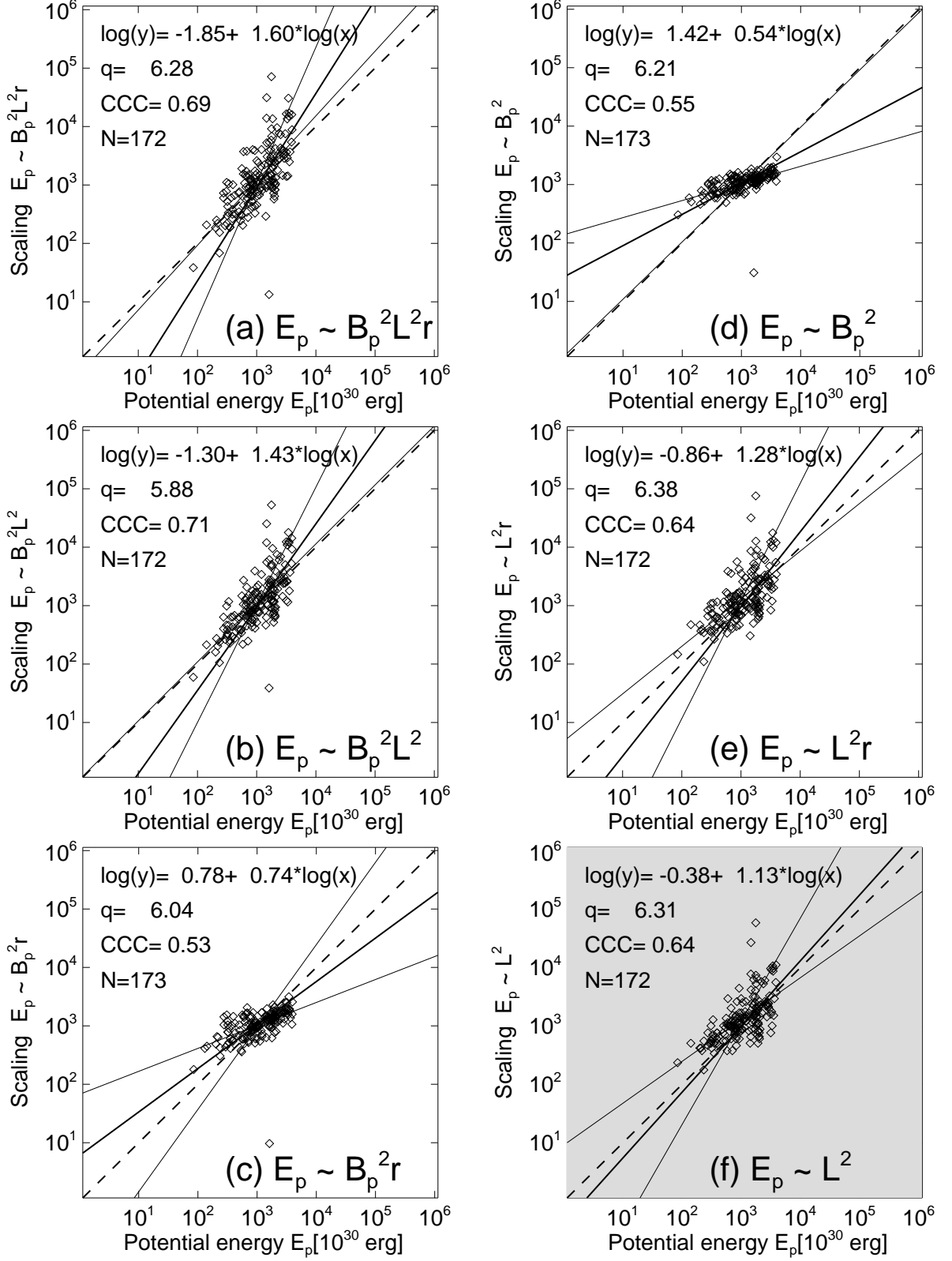


**Figure 3.** Parameter correlations are shown for theoretical scaling relationships  $E_p^{theo}$  (y-axis) of the potential field energy of a flaring active region as a function of the observed values  $E_p^{obs}$ , for  $N = 172$  M- and X-class flare events (diamond symbols), along with linear regression fits, the geometric mean of two fits  $y(x)$  and  $x(y)$  (thick solid lines), uncertainties (thin solid lines), and equivalence (dashed lines). The six cases correspond to models with different choices of correlated parameters. Models that produce a slope that is consistent with the data are marked with grey areas. See also Table 1.

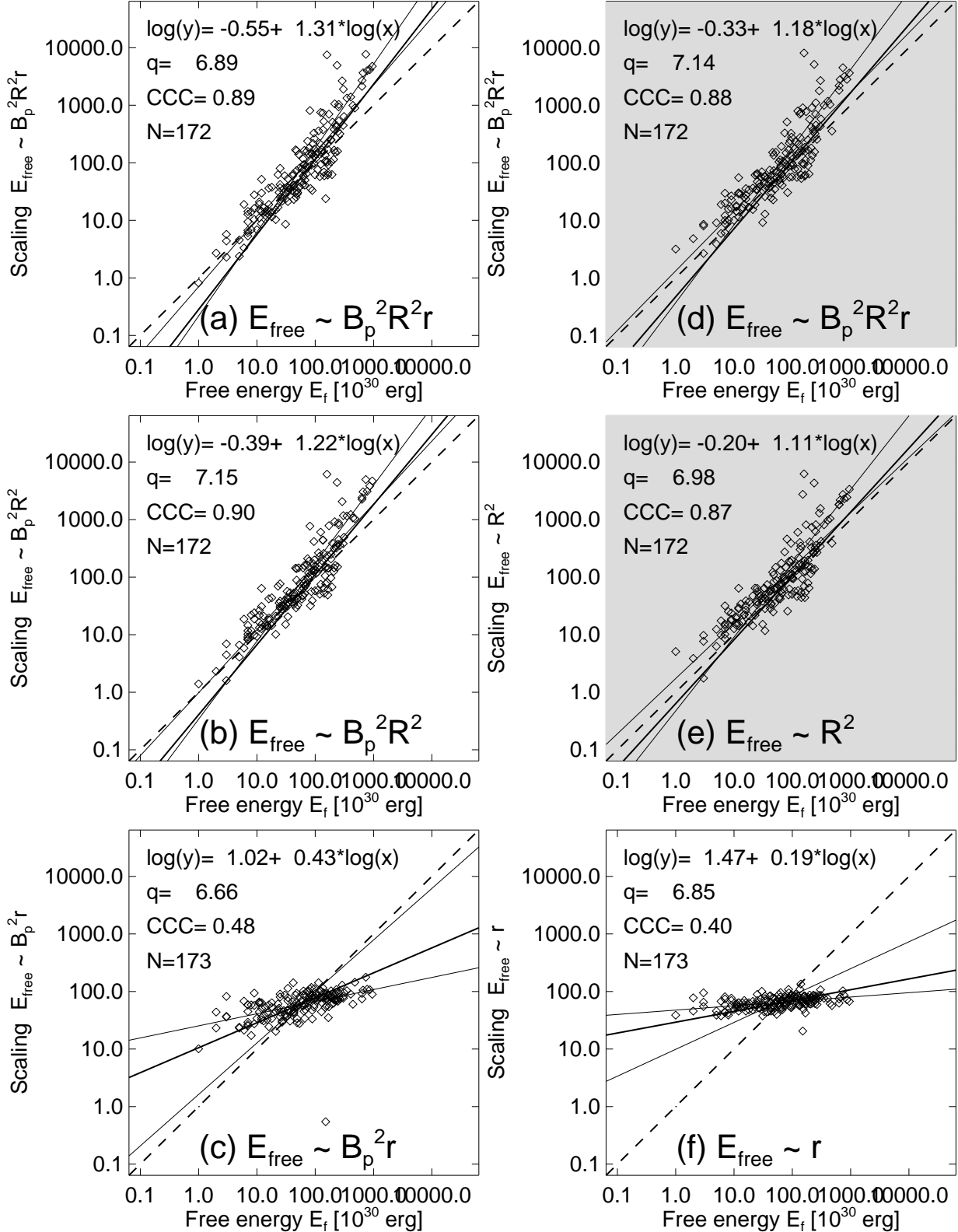


**Figure 4.** Parameter correlations are shown for the theoretical scaling relationships  $E_{free}^{theo}$  (y-axis) of the free magnetic energy as a function of the observed values  $E_{free}^{obs}$  for  $N = 173$  M- and X-class flare events (diamond symbols). Otherwise similar representation as in Fig. 3.

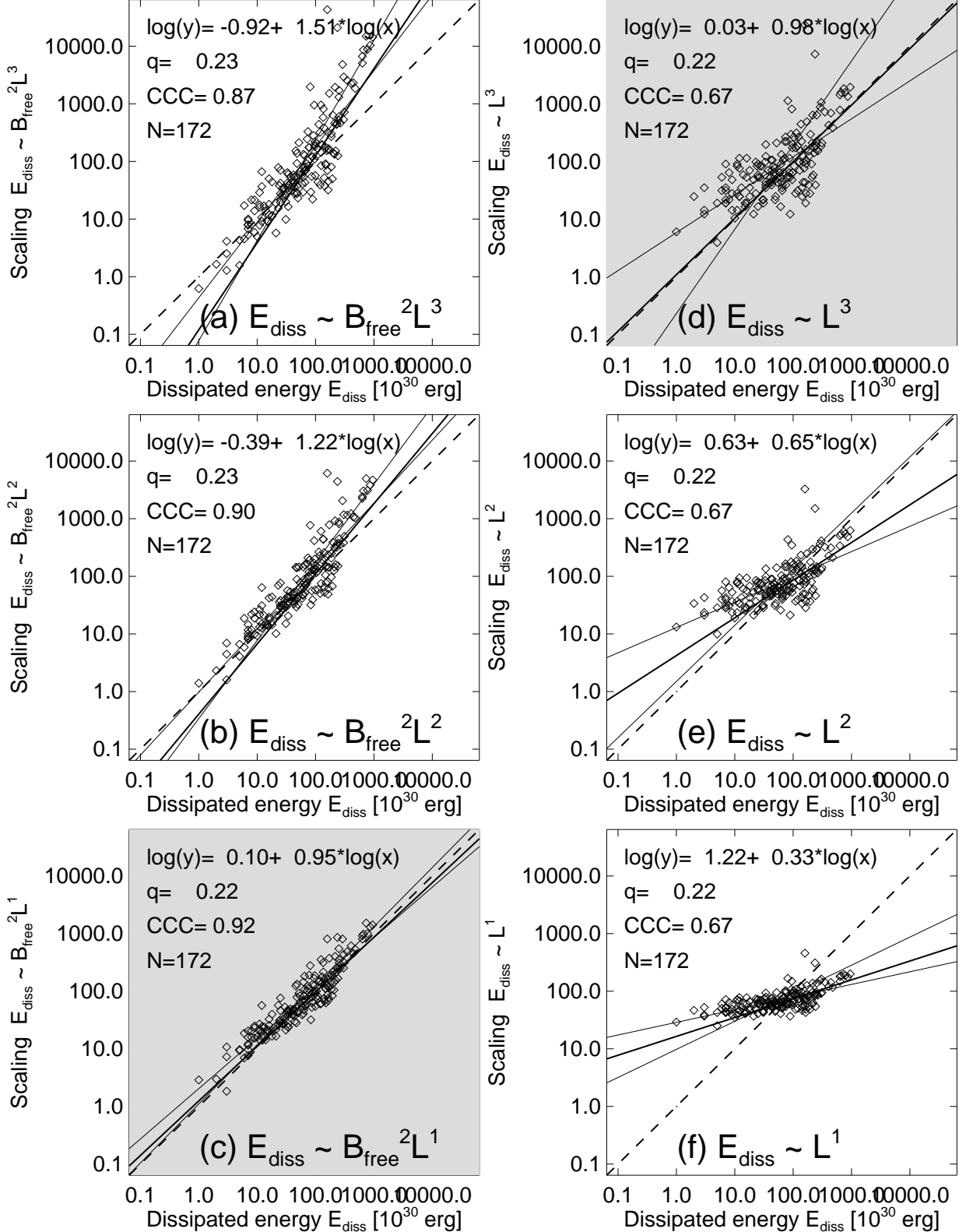


**Figure 5.** Parameter correlations of 6 Petschek-type models are shown for the theoretical scaling relationships  $E_d^{theo}$  (y-axis) of the dissipated magnetic energy as a function of the observed values  $E_d^{obs}$  for  $N = 172$  M- and X-class flare events (diamond symbols). Otherwise similar representation as in Fig. 4.

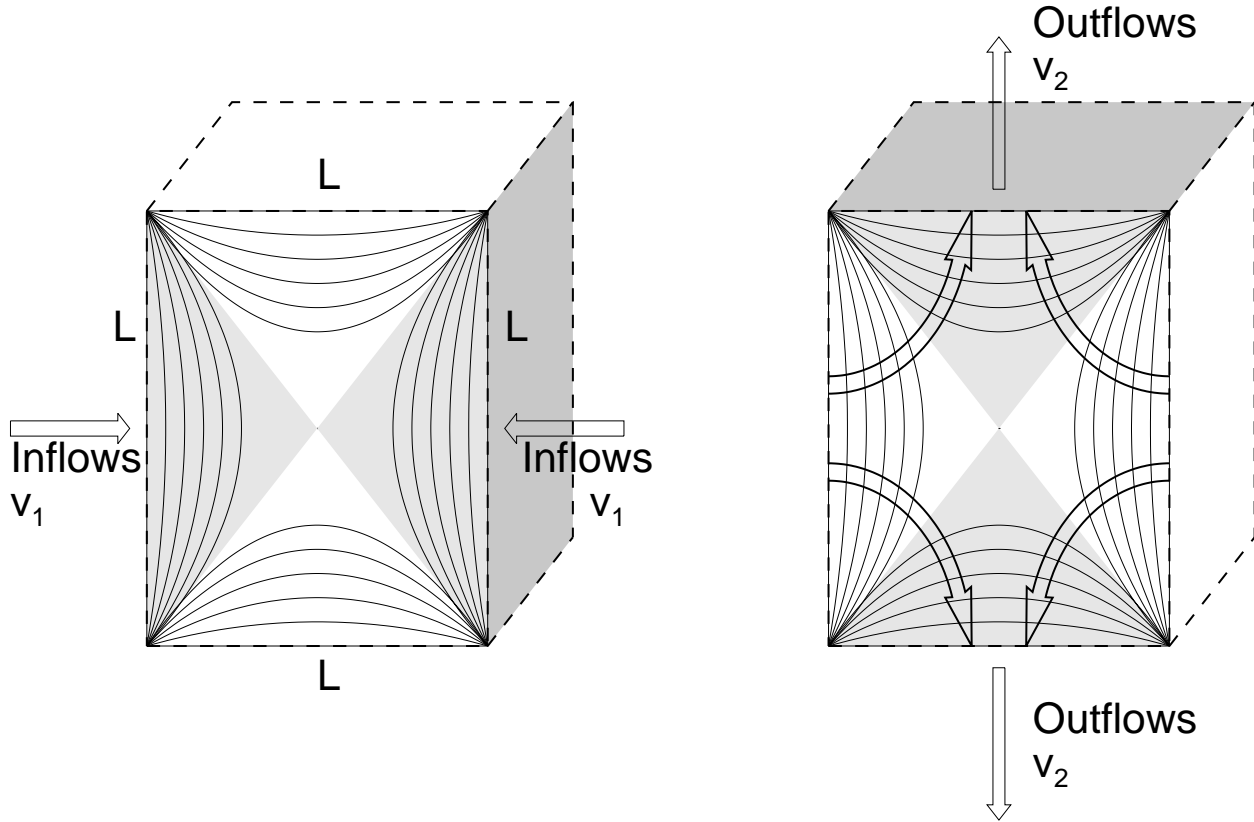


**Figure 6.** A schematic of the Petschek magnetic reconnection process, showing the horizontally directed inflows  $v_1$  that drive the reconnection (left panel), and the vertical outflows  $v_2$  in upward and downward direction from the central X-point (right panel). The 3-D box (dashed lines) with a length scale  $L$  in all directions mark the magnetic diffusion region.

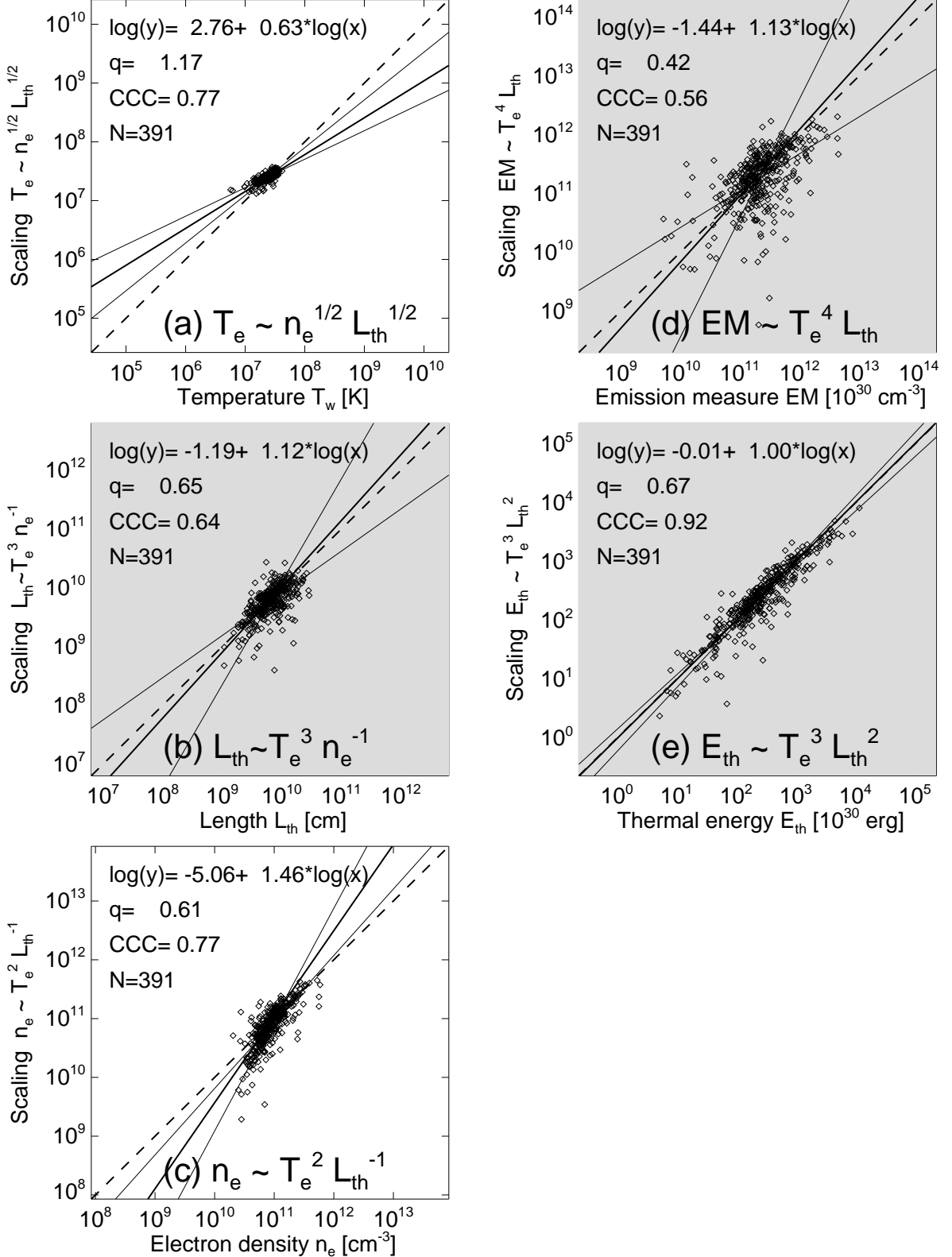


**Figure 7.** Correlations of five Rosner-Tucker-Vaiana (RTV) parameters are shown in form of the observed values on the x-axis versus the theoretically predicted scaling relationships on the y-axis, for  $N = 391$  M- and X-class flare events (diamond symbols). Otherwise similar representation as in Figs. (3)-(5).

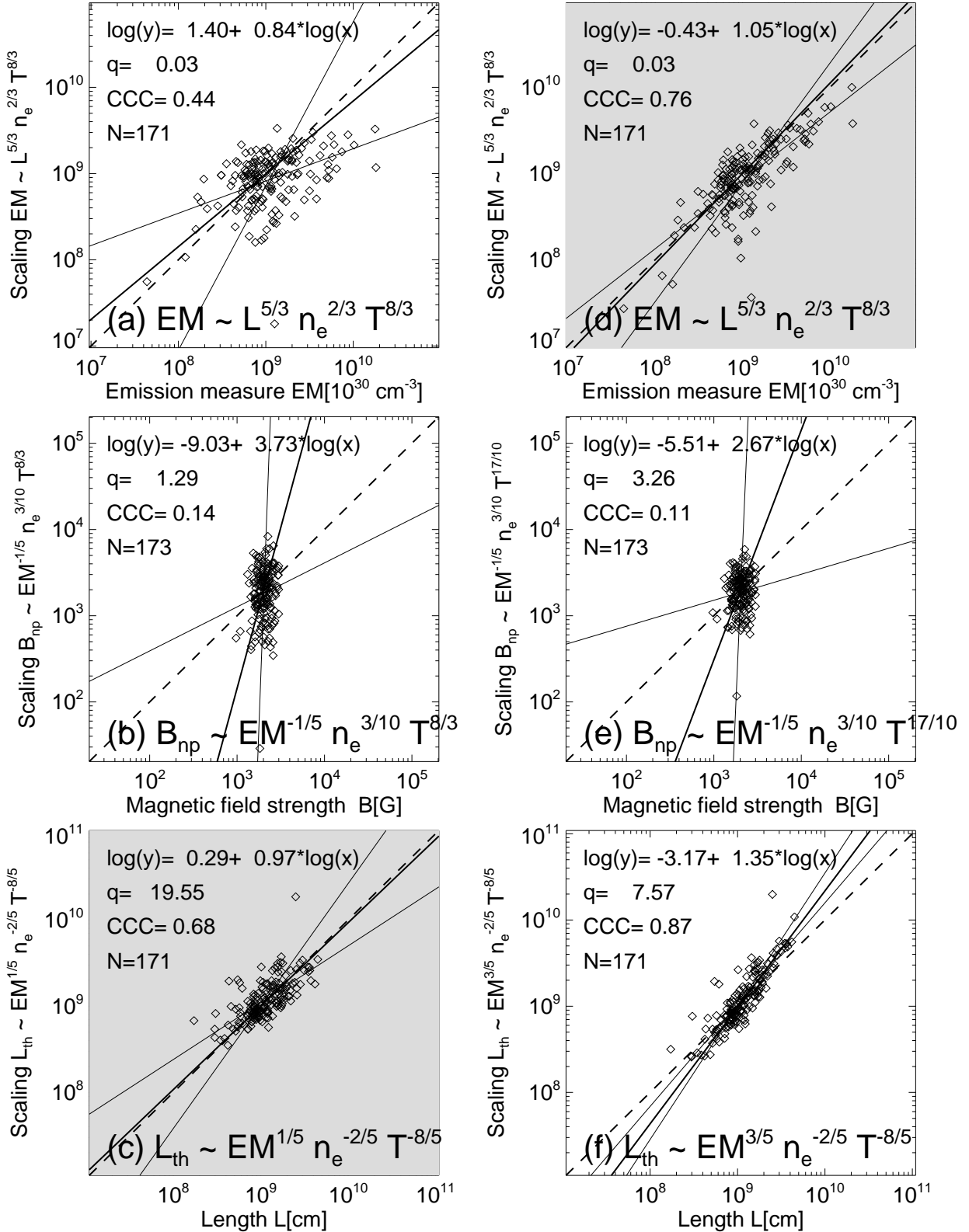


**Figure 8.** Correlations of four parameters of the Shibata-Yokoyama reconnection model are shown in form of the observed values on the x-axis versus the theoretically predicted scaling relationships on the y-axis, for  $N = 173$  M- and X-class flare events (diamond symbols). Otherwise similar representation as in Figs. (3)-(5).